



Hadron Correlations Measured with ALICE

Jan Fiete Grosse-Oetringhaus¹

CERN, 1211 Geneva 23, Switzerland

Abstract

Angular particle correlations are a powerful tool to study collective effects and in-medium jet modification as well as their interplay in the hot and dense medium produced in central heavy-ion collisions. We present measurements of two-particle angular correlations of inclusive charged and identified particles performed with the ALICE detector. The near-side peak in the short-range correlation region is quantitatively analyzed: while the rms of the peak in ϕ -direction is independent of centrality within uncertainties, we find a significant broadening in η -direction from peripheral to central collisions. The particle content of the near-side peak is studied finding that the p/π ratio of particles associated to a trigger particle is much smaller than the one in the bulk of the particles and consistent with fragmentation of a parton in vacuum.

Keywords: heavy-ion collisions, two-particle correlations, near-side jet peak, jet broadening, proton over pion ratio

1. Introduction

In central heavy-ion collisions at the LHC strong jet quenching has been reported by ALICE, ATLAS and CMS. The suppression of high- p_T particles quantified by the nuclear modification factor R_{AA} drops as far as 0.14 [1, 2]. Further, a strong di-jet energy asymmetry has been reported [3, 4], while the quenched energy reappears primarily at low to intermediate p_T (0.5-8 GeV/c) and also outside the jet cone [4]. The measurement of the yield of particles associated to a high- p_T trigger particle (8-15 GeV/c) quantified by I_{AA} shows a suppression on the away side and a mild enhancement on the near side indicating that medium-induced jet modifications can also be expected on the near side [5].

It is interesting to study the low to intermediate p_T region where the quenched energy reappears with the aim of constraining jet quenching mechanisms. Further, measurements in this p_T region allow to quantify interactions of high energetic partons and branched-off partons with the collectivity-dominated bulk.

Full jet reconstruction for jets with a transverse momentum of less than 10-20 GeV/c is very difficult due to the large backgrounds [6]. Two-particle angular correlations are a powerful alternative in this regime. This paper presents results from two-particle correlations which allow to extract a small signal over a large background stemming from collective effects and pure combinatorics.

Email address: jgrosseo@cern.ch (Jan Fiete Grosse-Oetringhaus)

¹for the ALICE collaboration

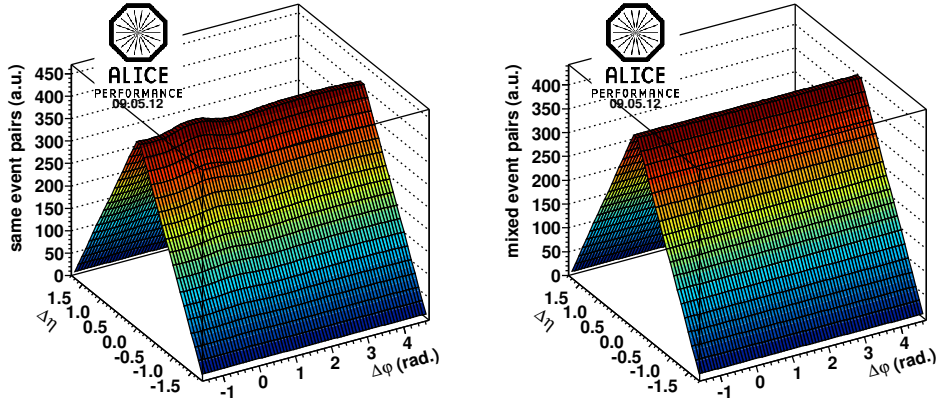


Figure 1: Correlation constructed from pairs of particles from the same event (left panel) and mixed events (right panel).

16 2. Detector & Data Sample

17 The ALICE detector is described in detail in [7]. The Inner Tracking System (ITS) and the Time Projection
 18 Chamber (TPC) are used for vertex finding and tracking. The collision centrality is determined with the forward
 19 scintillators (VZERO) at $-1.7 < \eta < -3.7$ and $2.8 < \eta < 5.1$. The main tracking detector is the TPC which
 20 allows reconstruction of good-quality tracks with a pseudorapidity coverage of $|\eta| < 1.0$ uniform in azimuth. The
 21 reconstructed vertex is used to select primary track candidates and to constrain the p_T of the track. For particle
 22 identification (PID) the specific energy loss measured in the TPC as well as the time of flight measured by the TOF
 23 system is used.

24 In the presented analysis about 15 million minimum-bias Pb–Pb events recorded in fall 2010 at $\sqrt{s_{NN}} = 2.76$ TeV
 25 as well as 55 million pp events from March 2011 ($\sqrt{s} = 2.76$ TeV) are used. These include only events where the TPC
 26 was fully efficient to ensure uniform azimuthal acceptance. Events are accepted which have a reconstructed vertex
 27 less than 7 cm from the nominal interaction point in beam direction. Tracks are selected by requiring at least 70 (out of
 28 up to 159) associated clusters in the TPC, and a χ^2 per space point of the momentum fit smaller than 4 (with 2 degrees
 29 of freedom per space point). In addition, tracks are required to originate from within 2.4 cm (3.2 cm) in transverse
 30 (longitudinal) distance from the primary vertex.

31 The data is corrected for tracking efficiency and contamination by secondary particles using the HIJING [8] and
 32 PYTHIA [9] event generators followed by particle transport and detector simulation based on GEANT3 [10].

33 3. Two-Particle Angular Correlations

34 The associated per trigger yield is measured as a function of the azimuthal angle difference $\Delta\phi = \phi_1 - \phi_2$ and
 35 pseudorapidity difference $\Delta\eta = \eta_1 - \eta_2$:

$$36 \frac{d^2 N}{d\Delta\phi d\Delta\eta}(\Delta\phi, \Delta\eta) = \frac{1}{N_{\text{trig}}} \frac{d^2 N_{\text{assoc}}}{d\Delta\phi d\Delta\eta} \quad (1)$$

37 where N_{assoc} is the number of particles associated to a number of trigger particles N_{trig} . This quantity is measured for
 38 different ranges of trigger $p_{T,\text{trig}}$ and associated transverse momentum $p_{T,\text{assoc}}$ and in bins of centrality.

39 Two-track efficiency and acceptance are assessed by using a mixed-event technique: the differential yield defined
 40 in Eq. (1) is also constructed for pairs of particles from different events. By definition all physical correlations are
 41 removed while those e.g. related to the acceptance remain. The events mixed with each other are selected with similar
 centralities and z -vertex positions. The angular correlation constructed from particles within the same event as well

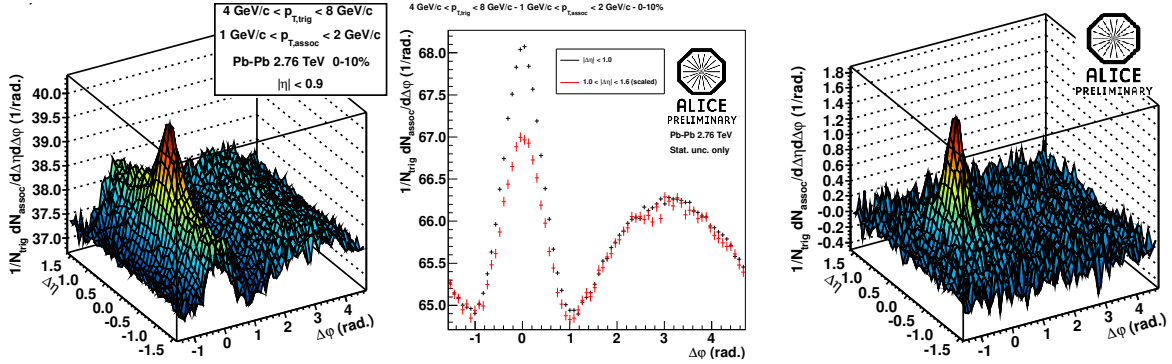


Figure 2: Left panel: per-trigger yield; middle panel: projection to $\Delta\varphi$ in $|\Delta\eta| < 1$ (black) and $|\Delta\eta| > 1$ (red); right panel: subtracted per-trigger yield.

42 as with mixed events are presented in Figure 1. A typical triangular shape is obtained in $\Delta\eta$ originating from the
 43 limited η -acceptance of the detector. Due to the uniform acceptance of the detector in ϕ , no significant structures can
 44 be observed in $\Delta\varphi$. Dividing those two distributions after proper normalization of the mixed-event distribution
 45 in the per-trigger yield, see e.g. the left panel in Figure 2, the quantity which is studied in the following.

46 To correct for efficiency losses in case of particles being spatially very close in the detector volume a cut on the
 47 spatial separation in the active volume of the TPC is performed. Applying this cut consistently in the same and mixed
 48 event distributions recovers the particles lost due to the detector inefficiency.

49 3.1. Near-Side Peak Shapes

50 A typical per-trigger yield is shown in the left panel of Figure 2. Visible are the near-side peak concentrated
 51 around $\Delta\varphi = \Delta\eta = 0$ sitting on top of a ridge structure around $\Delta\varphi = 0$ elongated in $\Delta\eta$ whose origin is flow. On the
 52 away-side around $\Delta\varphi = \pi$, a ridge mostly independent of $\Delta\eta$ can be observed, consisting of the recoil jet peak and the
 53 modulation from flow. The per-trigger yield has quite a large (flat) pedestal compared to the signal modulations.

54 We study the shape of the near-side jet peak by subtracting $\Delta\eta$ -independent effects. Those are estimated in the
 55 long-range correlation region at $|\Delta\eta| > 1$ and subtracted from the region $|\Delta\eta| < 1$. The center panel of Figure 2 shows
 56 the projection to $\Delta\varphi$ in $|\Delta\eta| > 1$ (red) and $|\Delta\eta| < 1$ (black). The difference between the two is the signal to be studied.
 57 By construction this procedure removes the away-side peak which is to a good approximation $\Delta\eta$ independent. The
 58 right panel of Figure 2 shows the subtracted per-trigger yield.

59 The near-side peaks are fitted with a superposition of 2 Gaussians which have their center at $\Delta\varphi = \Delta\eta = 0$. Such
 60 a fit function is chosen because it reproduces the features of the data in most bins ($\chi^2/ndf \approx 1.1 - 1.4$). We use the
 61 fit parameters to calculate the rms (equal to the variance, σ , for distributions centered at 0) of the distribution. In
 62 addition, we calculate the rms directly from the distribution as well as the excess kurtosis² K which is a measure of
 63 the peakedness of the distribution.

64 Figure 3 presents the rms in $\Delta\varphi$ (left panel) and $\Delta\eta$ (right panel) as a function of centrality; also shown are the
 65 results for pp collisions (shown at a centrality of 100). The rms in $\Delta\varphi$ direction is rather independent of centrality
 66 while there is a significant increase in the rms in $\Delta\eta$ direction towards central collisions. For peripheral and pp
 67 collisions, the rms is similar in $\Delta\varphi$ and $\Delta\eta$, e.g. about 0.4 for the lowest p_T bin studied. It increases in $\Delta\eta$ up
 68 to about 0.6 for 0-10% centrality. A similar relative increase is seen for the other p_T bins studied. Generally, the
 69 parameters continue smoothly from peripheral collisions to pp collisions. In [11] it was suggested that the interplay of
 70 longitudinal flow with a fragmenting high p_T parton can lead to such an asymmetric peak shape. The lines in Figure 3
 71 are from models: for Pb-Pb AMPT (A MultiPhase Transport Code; version 2.25 with string melting) simulations
 72 [12, 13] which describe collective effects in heavy-ion collisions at the LHC reasonably well, are shown, while for pp

²Kurtosis $K = \mu_4/\mu_2^2 - 3$; μ_n being the n^{th} moment.

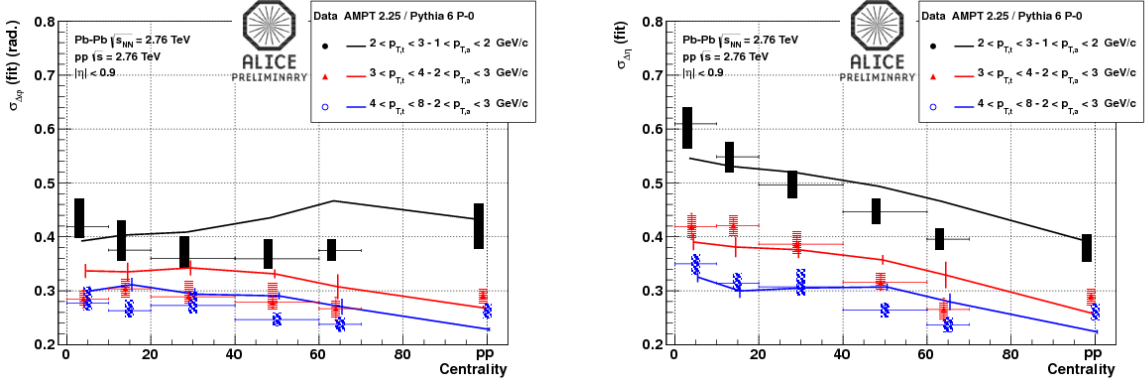


Figure 3: rms in $\Delta\varphi$ (left panel) and $\Delta\eta$ (right panel) calculated from the fit parameters for different p_T bins as function of centrality. Shown are data (points) and AMPT and PYTHIA Monte Carlo simulations (lines).

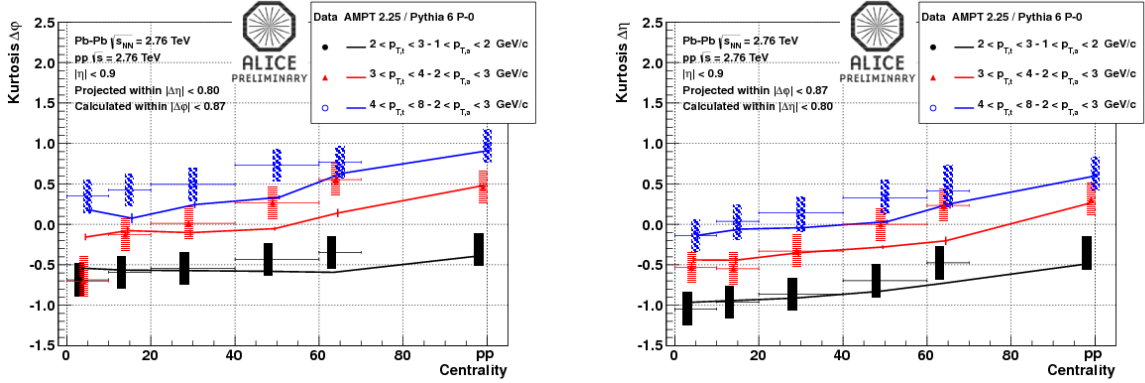


Figure 4: Kurtosis in $\Delta\varphi$ (left panel) and $\Delta\eta$ (right panel) calculated from the fit parameters for different p_T bins as function of centrality. Shown are data (points) and AMPT and PYTHIA Monte Carlo simulations (lines).

73 PYTHIA 6.4 [9] with the tune Perugia-0 [14] is presented. These describe the rms in $\Delta\varphi$ and $\Delta\eta$ qualitatively and to
 74 some extent also quantitatively. AMPT models the interplay of a jet with flow with partonic and hadronic rescattering.
 75 Figure 4 shows the Kurtosis in $\Delta\varphi$ and $\Delta\eta$ direction. It increases from central to peripheral collisions: the near-side is
 76 less peaked towards central collisions. Also the Kurtosis is well described by AMPT and PYTHIA.

77 The lowest p_T bin shows an interesting structure for the most central collisions presented in Figure 5: in $\Delta\eta$
 78 direction a departure from a Gaussian is observed. The peak shows a flat top (an indication for a double-humped
 79 structure can be seen which is not significant, though). This feature is also reproduced in AMPT. It will be interesting
 80 to explore the reasons for such effects in AMPT. More details about this analysis can be found in [15].

81 4. p/π Ratio in Jet and Bulk

82 Baryon over meson ratios differ significantly between central heavy-ion and pp collisions. E.g. the Λ/K_S^0 ratio
 83 increases up to about 1.5 in central Pb–Pb collisions at the LHC, while it is about 0.5 in pp collisions [16]. We study
 84 particle ratios in the near-side peak by performing two-particle correlations with identified particles. This allows to
 85 separate the bulk of the particles from those associated to a high- p_T trigger particle.

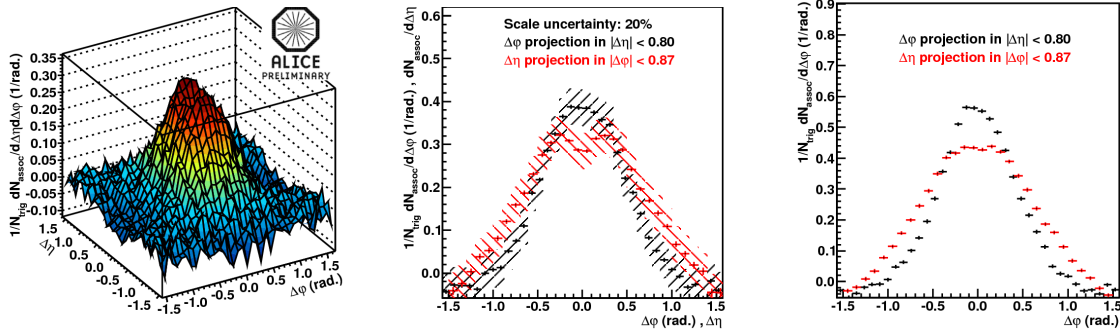


Figure 5: Per-trigger yield for $2 \text{ GeV}/c < p_{T,\text{trig}} < 3 \text{ GeV}/c$, $1 \text{ GeV}/c < p_{T,\text{assoc}} < 2 \text{ GeV}/c$ and 0-10% centrality. The left panel shows the data; the middle panel shows projections of the data to $\Delta\phi$ (black) and $\Delta\eta$ (red) while the right panel shows the same projections from AMPT simulations.

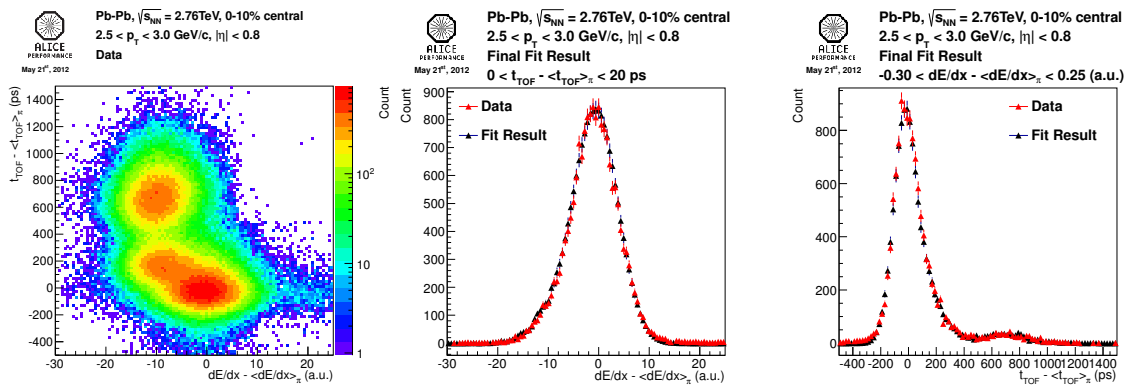


Figure 6: Illustration of the particle identification technique. Left panel: yield of particles as function of measured minus expected time of flight vs measured minus expected specific energy loss; middle panel: projection of the data (black) and the fit function (red) to the specific energy loss axis; right panel: projection of the data (black) and the fit function (red) to the time of flight axis.

86 The particle identification is performed by exploiting specific energy loss as well as time of flight information.
 87 The left panel of Figure 6 shows an example for one p_T bin and the pion hypothesis. The x and y axis show the
 88 measured specific energy loss and time of flight, respectively, minus the expected one. For each abundant particle
 89 species, pions (around 0, by construction), kaons and protons, a corresponding peak is observed. The pion peak is
 90 approximately Gaussian while the others are distorted because the incorrect (pion) mass hypothesis is used also for
 91 those particles. These peaks are fitted to extract the particle yields. For the pion peak a Gaussian (plus an exponential
 92 tail towards positive t_{TOF}) is used while Monte Carlo templates are used for the other ones. The center and right panels
 93 of Figure 6 show projections of the data and fit function to the specific energy loss and time of flight axis, respectively.
 94 This procedure is performed for each particle species, i.e. the corresponding mass hypothesis is used, to extract the
 95 yield for that species. These yields are corrected for tracking and PID efficiency based on Monte Carlo simulations.
 96 No correction for feeddown from e.g. Λ has been applied.

97 Similarly to the previous discussed analysis the yields in the long-range correlation region are subtracted from the
 98 yields in the near-side peak region. The left panel of Figure 7 shows the regions defined in the $\Delta\phi$ - $\Delta\eta$ plane: the *bulk*
 99 *I* and *II* regions are used to estimate the background under the *peak region*. The remaining yield in the peak region is
 100 the yield correlated to the trigger particle and is called *jet* yield in the following. More details about this analysis can
 101 be found in [17].

102 The particle yields are used to calculate the p/π ratio as a function of $p_{T,\text{assoc}}$ for $5 \text{ GeV}/c < p_{T,\text{trig}} < 10 \text{ GeV}/c$,

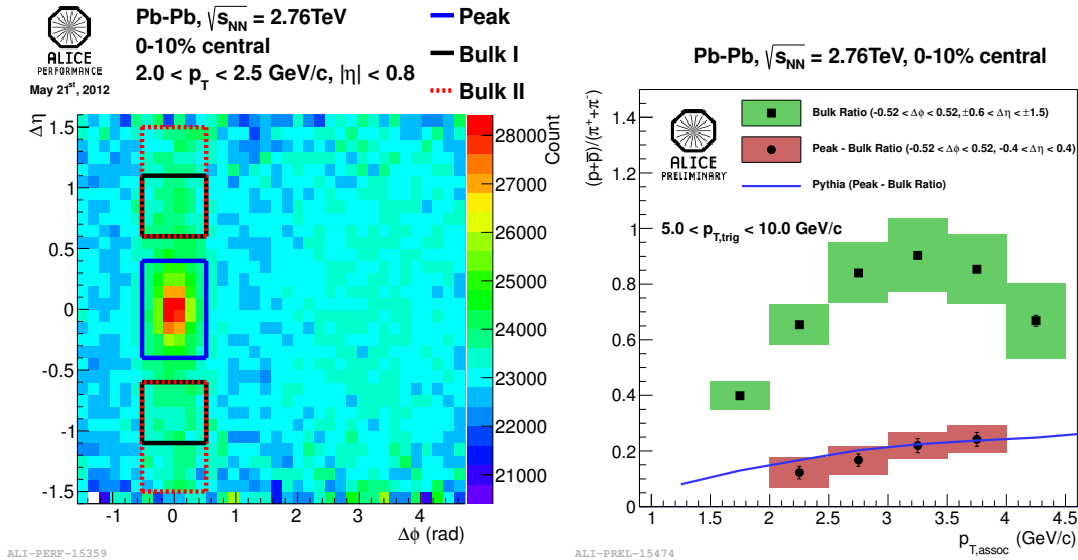


Figure 7: Left panel: regions in the $\Delta\phi$ - $\Delta\eta$ plane where the yields for the peak and bulk are extracted (for details see text). Right panel: p/π ratio in the bulk (squares) and peak–bulk (circles) regions compared to the PYTHIA expectation (line).

103 shown in the right panel of Figure 7. The p/π ratio in the bulk region increases up to about 1 at about 3 GeV/c and is
 104 similar to the inclusive one calculated over all particles (not shown). The ratio of the particles associated to the jet is
 105 significantly smaller (maximum at about 0.3) and consistent with the PYTHIA simulation (version 6.4 default tune)
 106 which assumes vacuum fragmentation. Hence, this observable shows no evidence for medium-induced modification
 107 of the jet fragmentation in central Pb–Pb collisions.

108 5. Summary

109 Two-particle correlations have been used to quantify the effects of the hot and dense medium on the near-side
 110 peak associated to a trigger particle with a transverse momentum in the range 2–10 GeV/c. The near-side peak shape
 111 has been studied revealing that the symmetric peak in peripheral and pp collisions gets asymmetric in central Pb–Pb
 112 collisions: the rms in $\Delta\eta$ is significantly larger than in $\Delta\phi$. Rms and excess kurtosis are well reproduced by AMPT
 113 compatible with the interpretation that the interplay of jets with the flowing bulk is the origin of the found feature. The
 114 associated p/π ratio to a trigger particle has been found to be much smaller than the one in the bulk. The p/π ratio
 115 is compatible with simulations assuming vacuum fragmentation, i.e. no evidence for medium-induced modification
 116 of the jet fragmentation is observed in the studied p_T regime. In summary, two interesting observations have been
 117 presented and a continuation as well as combination of these studies seems very promising to gain further insight into
 118 the jet quenching mechanism occurring in heavy-ion collisions at the LHC.

119 References

- 120 [1] K. Aamodt, et al., Suppression of Charged Particle Production at Large Transverse Momentum in Central Pb–Pb Collisions at $\sqrt{s_{NN}} = 2.76$
 121 TeV, Phys.Lett. B696 (2011) 30–39. arXiv:1012.1004, doi:10.1016/j.physletb.2010.12.020.
 122 [2] S. Chatrchyan, et al., Study of high- p_T charged particle suppression in PbPb compared to pp collisions at $\sqrt{s_{NN}}=2.76$ TeV, Eur.Phys.J.
 123 C72 (2012) 1945. arXiv:1202.2554, doi:10.1140/epjc/s10052-012-1945-x.
 124 [3] G. Aad, et al., Observation of a Centrality-Dependent Dijet Asymmetry in Lead-Lead Collisions at $\sqrt{s_{NN}}=2.76$ TeV with the ATLAS
 125 Detector at the LHC, Phys.Rev.Lett. 105 (2010) 252303. arXiv:1011.6182, doi:10.1103/PhysRevLett.105.252303.
 126 [4] S. Chatrchyan, et al., Observation and studies of jet quenching in PbPb collisions at nucleon-nucleon center-of-mass energy = 2.76 TeV,
 127 Phys.Rev. C84 (2011) 024906. arXiv:1102.1957, doi:10.1103/PhysRevC.84.024906.

- 128 [5] K. Aamodt, et al., Particle-yield modification in jet-like azimuthal di-hadron correlations in Pb-Pb collisions at $\sqrt{s_{NN}} = 2.76$ TeV,
129 Phys.Rev.Lett. 108 (2012) 092301. [arXiv:1110.0121](#), [doi:10.1103/PhysRevLett.108.092301](#).
- 130 [6] B. Abelev, et al., Measurement of Event Background Fluctuations for Charged Particle Jet Reconstruction in Pb-Pb collisions at $\sqrt{s_{NN}} = 2.76$
131 TeV, JHEP 1203 (2012) 053. [arXiv:1201.2423](#), [doi:10.1007/JHEP03\(2012\)053](#).
- 132 [7] K. Aamodt, et al., The ALICE experiment at the CERN LHC, JINST 3 (2008) S08002. [doi:10.1088/1748-0221/3/08/S08002](#).
- 133 [8] X.-N. Wang, M. Gyulassy, HIJING: A Monte Carlo model for multiple jet production in p p, p A and A A collisions, Phys.Rev. D44 (1991)
134 3501–3516. [doi:10.1103/PhysRevD.44.3501](#).
- 135 [9] T. Sjostrand, S. Mrenna, P. Z. Skands, PYTHIA 6.4 Physics and Manual, JHEP 05 (2006) 026. [arXiv:hep-ph/0603175](#), [doi:10.1088/](#)
136 [1126-6708/2006/05/026](#).
- 137 [10] R. Brun, F. Bruyant, M. Maire, A. C. McPherson, P. Zancarini, GEANT3CERN-DD-EE-84-1.
- 138 [11] N. Armesto, C. A. Salgado, U. A. Wiedemann, Measuring the collective flow with jets, Phys.Rev.Lett. 93 (2004) 242301. [arXiv:hep-ph/](#)
139 [0405301](#), [doi:10.1103/PhysRevLett.93.242301](#).
- 140 [12] Z.-W. Lin, C. M. Ko, B.-A. Li, B. Zhang, S. Pal, A Multi-phase transport model for relativistic heavy ion collisions, Phys.Rev. C72 (2005)
141 064901. [arXiv:nucl-th/0411110](#), [doi:10.1103/PhysRevC.72.064901](#).
- 142 [13] J. Xu, C. M. Ko, Pb-Pb collisions at $\sqrt{s_{NN}} = 2.76$ TeV in a multiphase transport model, Phys.Rev. C83 (2011) 034904. [arXiv:1101.2231](#),
143 [doi:10.1103/PhysRevC.83.034904](#).
- 144 [14] P. Z. Skands, Tuning Monte Carlo Generators: The Perugia Tunes, Phys. Rev. D82 (2010) 074018. [arXiv:hep-ph/1005.3457](#), [doi:](#)
145 [10.1103/PhysRevD.82.074018](#).
- 146 [15] A. Morsch for the ALICE collaboration, Jet-like near-side peak shapes in Pb–Pb collisions at $\sqrt{s_{NN}} = 2.76$ TeV with ALICE, [arXiv:](#)
147 [1207.7187](#).
- 148 [16] I. Belikov, K0s and Lambda production in Pb–Pb collisions with the ALICE experiment. [arXiv:1109.4807](#).
- 149 [17] M. Veldhoen for the ALICE collaboration, p/π Ratio in Di-Hadron Correlations. [arXiv:1207.7195](#).



Available online at www.sciencedirect.com



Nuclear Physics A 00 (2021) 1–1



www.elsevier.com/locate/nuclphysa

Abstract

Keywords:

1.

arXiv:1208.1445v1 [nucl-ex] 7 Aug 2012